Published in final edited form as:
Sci Robot. 2017 March 15; 2(4): . doi:10.1126/scirobotics.aal4916.

Instrument flight to the inner ear

Stefan Weber[1,*], **Kate Gavaghan**[1], **Wilhelm Wimmer**[1,2], **Tom Williamson**[1], **Nicolas Gerber**[1], **Juan Anso**[1], **Brett Bell**[1], **Arne Feldmann**[3], **Christoph Rathgeb**[1], **Marco Matulic**[1], **Manuel Stebinger**[1], **Daniel Schneider**[1], **Georgios Mantokoudis**[2], **Olivier Scheidegger**[4], **Franca Wagner**[5], **Martin Kompis**[2], **Marco Caversaccio**[1,2]

[1]ARTORG Center for Biomedical Engineering Research, University of Bern

[2]Department of Otorhinolaryngology, Head and Neck Surgery, Inselspital, Bern University Hospital

[3]Institute for Surgical Technologies and Biomechanics, University of Bern

[4]Department Neurology, Inselspital, Bern University Hospital

[5]Institute of Diagnostic and Interventional Neuroradiology, Inselspital, Bern University Hospital

Abstract

Surgical robot systems can work beyond the limits of human perception, dexterity and scale making them inherently suitable for use in microsurgical procedures. However, despite extensive research, image-guided robotics applications for microsurgery have seen limited introduction into clinical care to date. Among others, challenges are geometric scale and haptic resolution at which the surgeon cannot sufficiently control a device outside the range of human faculties. Mechanisms are required to ascertain redundant control on process variables that ensure safety of the device, much like instrument-flight in avionics. Cochlear implantation surgery is a microsurgical procedure, in which specific tasks are at sub-millimetric scale and exceed reliable visuo-tactile feedback. Cochlear implantation is subject to intra- and inter-operative variations, leading to potentially inconsistent clinical and audiological outcomes for patients. The concept of robotic cochlear implantation aims to increase consistency of surgical outcomes such as preservation of residual hearing and reduce invasiveness of the procedure. We report successful image-guided, robotic CI in human. The robotic treatment model encompasses: computer-assisted surgery planning, precision stereotactic image-guidance, in-situ assessment of tissue properties and multipolar neuromonitoring (NM), all based on in vitro, in vivo and pilot data. The model is expandable to integrate additional robotic functionalities such as cochlear access and electrode insertion. Our results demonstrate the feasibility and possibilities of using robotic technology for

[*]Corresponding author stefan.weber@artorg.unibe.ch.

Author contributions: S.W. and M.C. created the study design. B.B., T.W., K.G., N.G., W.W. M.S., A.F., J.A., C.R., D.S., S.W., developed significant hardware and software components, carried out accuracy experiments and analysed the data, and performed in-vivo animal testing. All authors had significant clinical and technical responsibilities during the clinical trial. All authors reviewed the manuscript.

Competing interests: B.B., T.W., S.W. are inventors on the related patent: EP2666248; A.F., S.W. are inventors on the related patent EP16153033.S.W. is co-founder, shareholder and advisor to the board and M.M. is chief technology officer and shareholder of CAScination AG (Bern Switzerland), a company that is developing robotic cochlear implantation technology. MC is a member of the scientific advisory board and M.K. received travel funding from MED-EL GmbH (Innsbruck, Austria), a cochlear implant company.

Data and materials availability: There are no material transfer agreements or restrictive patents.

Europe PMC Funders Author Manuscripts

microsurgery on the lateral skull base. It has the potential for benefit in other microsurgical domains for which there is no task-oriented, robotic technology available at present.

1 Introduction

Current robotic surgical technology augments the surgeon's toolkit and permits execution of human-like tasks with superior accuracy, consistency or speed. Image-guided and model based robotic systems are commissioned in surgical and interventional domains as diverse as orthopedics (Pearle et al. 2009), neurosurgery (Smith et al. 2016), radio surgery (Lunsford et al. 1989), and interventional oncology (Koethe et al. 2014). Surgical robots are used for tele-manipulation of laparoscopic instruments in general (Xiong et al. 2012), urological (Close et al. 2013), gynecological surgery (Reza et al. 2010) and ophthalmic surgery (de Smet et al. 2016). Their application is often with compromised visual perception and diminished tactile information and therefore with reduced effectiveness. During the operation of robotic technology in surgery, a high-level control loop needs to be closed at all times via the human observer using direct visual, microscopic or endoscopic inspection. Hence, performance of robot operation is limited to human sensing, processing and execution capabilities (Brett et al. 2014) and as a result, the "super-human" sensing and actuation features inherent in robotic devices remain largely unharnessed in today's Operating Rooms (ORs) (Marcus et al. 2013). Next generation robotic devices will have to execute procedures reliably at geometric scales, temporal resolutions and safety levels beyond those possible for a human operator alone. If established, surgical robot technology that is capable of operation beyond the limitations of human sensing and tactile skills, can contribute to disruptive surgical procedures addressing as yet unmet clinical needs.

Cochlear implantation is an otologic microsurgery procedure in which a silicone wire with platinum electrodes is inserted into the cochlea. The electrode array is part of a cochlear implant (CI) providing hearing sensation to severe-to-profoundly deaf patients and some 65'000 CIs are implanted globally per year. Conventionally, surgeons are required to work at the limits of their visuo-tactile feedback and dexterity when accessing the middle-ear through a 30mm opening to place the electrode array (0.3-1 mm diameter) within the cochlea of the inner-ear, while at the same time avoiding unnecessary disturbances and pressure transients. Although surgical techniques were developed to preserve residual hearing during implantation ("soft surgery"), about 30-55% of patients suffer significant hearing loss in the implanted ear (Huarte and Roland 2014). This can be ascribed at least in part to variations in surgeon-operator experience, practice and method. It is our view that robotic technology has the potential to overcome these human operator limitations and allow reproducible, minimally invasive cochlear access and a controlled electrode insertion process. Thus, Robotic Cochlear Implantation (RCI) could lead to deliberate and accurate placement of the electrode in the inner ear, for higher consistency of residual hearing preservation and improved audiological outcomes. More importantly, the increased consistency of a robotic procedure potentially widens CI patient eligibility in the future.

Research on RCI has so far focused on the individual elements of the procedure such as image-based strategy planning (Nobel et al. 2012, Gerber et al. 2014, Wimmer et al. 2014a),

Europe PMC Funders Author Manuscripts

guided keyhole trajectory drilling using surgical templates (Labadie et al. 2005), industrial robotic manipulators (Federspil et al 2003, Xia et al. 2008, Danilchenko et al. 2011) and skull mounted passive kinematic structures (Kratchman et al. 2011, Kobler et al. 2015, Dillon et al 2015). Options for the reproducible creation of cochlear access using robotic force-feedback control (Brett et al. 2014) and the design of robotic electrode insertion systems (Miroir et al. 2012, Schurzig et al. 2012) have been addressed. Zhang et al. 2010 demonstrated the feasibility of deployment of steerable electrode arrays using robotic technology. In-vivo sensing and subsequent adaptation of a surgical plan for inserting perimodiolar electrode arrays was demonstrated Pile et al. (2014) together with the capability of failure prediction during the insertion process (Pile et al. 2016). Clark et al 2012 demonstrated efficacy of applying magnetically induced torque to the electrode array as a clinical strategy towards improved cochlear implant surgery. To date, Labadie (2014) has successfully combined several of the necessary elements that underpin a robotic CI technology suitable for clinical application and demonstrated the feasibility of geometrically constrained template drilling of a keyhole access in patients. Brett (2014) has put forward a robotic cochleostomy drill system, used in 3 patients, another necessary element in RCI.

Our work has focused on the development of a precise and safe approach for robotic middle ear access. In a step-wise process we addressed all stages of middle-ear access for RCI: a precise, stereotactically and image controlled drill process using a task-specific robotic technology (Bell 2013), secondary positional estimates using correlations of bone density and drill force (Williamson et al. 2013) and task-specific neuromonitoring to detect whether the robotic drilling process passes at a sufficient distance from the facial nerve (Ansó et al. 2016). Furthermore, specific parameters for drill forward thrust, pecking and rotational speed have been experimentally validated to ensure a heat-minimized drill process. These stages are designed to permit middle ear access that intends to create reproducibly a keyhole drill trajectory (diameter 1.5 to 2 mm) from the skull surface to a predefined target on the cochlea (Figure 1b). Finally, to enable an end-to-end, robotic cochlear implantation procedure, strategies for optimal electrode selection and sufficient placement of the cochlear implant electrode through the robotic keyhole have been developed and validated (Wimmer et al. 2014b).

Here we describe how our robotic treatment model is applied to our technology and then used to carry out our first robotic cochlear implantation successfully in a patient; consisting of computer assisted planning, subsequent robotic access to the middle ear followed by manual inner ear access and electrode insertion through the access created. Overall system setup, the clinical workflow, the results of the first intervention and the operation of the safety mechanisms are set out. The case presented also includes analysis to show preclinical feasibility and functional outcome.

2 Results

2.1 A general treatment model for robotic middle ear access

We have developed and implemented a robotic treatment model that consists of several active and passive interlocking elements to minimize the risk of structural and heat damage to the relevant anatomy. Passive mode safety is contributed by precision image-guidance and

by heat-minimized robotic drilling. Active mode safety includes: (1) a secondary position measurement based on correlation of bone density with applicable drilling force, (2) neuromonitoring and (3) intraoperative imaging (Figure 2 and Table 1). The geometric scale of the human ear and the precision required to operate in the proximity of critical anatomy necessitates the use of an image-guided surgical robot system. However, image-guidance models are prone to errors and inaccuracies (imaging, image annotation, patient-to-image registration, instruments calibration and tracking) and effective accuracy cannot be reliably verified using live cues from the robotic operating field as seen by the surgeon operator. Even more critical at this geometric scale, a surgeon operator is not equipped to monitor and judge the correct alignment of the robot's drill axis according to the plan, solely using visual inspection. Safety mechanisms must be in place that allow cross-comparison of any safety relevant information and ultimately warrant safe robot performance. Unlike robotic guiding devices (Kratchman et al. 2011) or surgical templates (Labadie et al. 2005) only robotic devices can collect and map sensor data spatially and temporally to drive a dynamically responsive safety system.

The general model implemented here is the foundation for a patient-specific, image-based, precision drill plan and consists of the geometric definition of the trajectory within the mastoid, parameter sets for the various drilling phases and risk mitigation actions such as intraoperative cone-beam computed tomography (CBCT) imaging, neuromonitoring and bone density measurements as well as relevant manual activities such as electrode insertion. The model is extendable to future requirements (i.e. additional robotic task such as robotic inner ear access and robotic electrode insertion), adaptable for other applications and is individually parameterized for each patient using a specific software based planning system, described below.

2.2 Clinical investigation

With approval from the local institutional review board (ethics commission of the Canton of Bern, Switzerland, KEK-BE 156/13) and national medical device regulatory body (Swissmedic 2013-MD-0042, EUDAMED CIV-13-12-011779) a clinical trial on the feasibility of the robotic approach commenced with a first patient in summer 2016. A 51-year-old female patient with bilateral deafness was elected for unilateral cochlear implantation in the right ear. Prior to study inclusion, a minimum distance of 0.4 mm between the planned drill tunnel, the facial nerve and the chorda tympani was confirmed using CT imagery acquired as part of the standard, preoperative CI clinical assessment protocol. The robotic cochlear implantation plan included a direct tunnel drilling to the middle ear, manual access to the cochlea via an extended round window approach and subsequent electrode placement. Microscopic visualization, electrode impedance, electrically evoked compound action potential measurements and postoperative CT images were used to confirm effective electrode array placement. Postoperative CT imaging was used to verify geometric accuracy of the drilled tunnel. Pre- and postoperative levels of facial nerve activity and taste sensation were measured and compared to ascertain effectiveness of the safety mechanisms employed.

2.3 The robotic procedure

After implanting four surgical fiducial screws for registration (2.2mm Ø × 5mm length, M-5243.05, Medartis, Switzerland) into the mastoid, the patient's lateral skull base was CT imaged (Siemens SOMATOM Definition Edge). A robotic treatment plan was created using a validated, custom software tool (Gerber et al 2014). Upon automatic detection of the fiducials and semi-automatic annotation of critical anatomical structures, a tunnel trajectory of 23mm with 0.5mm clearance to critical anatomical structures was defined. The proximal end of the trajectory was defined as the center of the cochlea's round window membrane. Risk mitigation actions (Table 1) as part of the robotic procedure were defined to be: a secondary trajectory pose measurement using a correlation of bone density with drill force (A1), intraoperative imaging at a level of 3mm before the facial nerve (A2) and during drilling past the facial nerve, five attempts of facial nerve stimulation and subsequent response measurements were carried out in spatial increments of 0.5 mm (A3). General preoperative, patient preparation involved placement of the patient's head in a dedicated headrest specifically designed to provide stable, non-invasive head fixation during drilling (Figure 3a).

Facial nerve monitoring (FNM) electrodes were attached to the facial muscles, and ground and stimulation return current electrodes to the upper chest (under the neck circumference, see Figure 3a) to allow neuromonitoring of the facial nerve during the procedure. Hardware preparation included attachment of the robot system to the OR table, connection to the control system and sterile draping. Initially, the patient's lateral skull was registered using the bone-anchored fiducial screws to allow for a transfer of the drill trajectory's entry point and the patient optical reference skull attachment point to the situs. The patient optical reference was mounted using a percutaneous 8mm bone screw. A retractor was placed to keep the area around the trajectory entry point accessible for the robot drill. A secondary, accuracy-optimized registration was performed immediately prior to drilling (fiducial registration error: 0.09mm). The robotic drilling was carried out according to the plan created in the procedural work-up and by strictly avoiding any physical movement of the patient (Figure 3b). Table 1 gives a summary and parameters of the drill process.

2.4 Implant management and electrode array insertion

On completion of the robotic drilling, the fiducial screws, the optical reference, and the robotic arm were removed from the situs. A tympanomeatal flap was created for additional visual and instrument access to the middle ear cavity (Wimmer et al. 2014b, Venail et al. 2015). A correct alignment of the tunnel with the round window was visually confirmed by endoscopic inspection. The tunnel was extensively rinsed to be cleaned from bone dust and blood. The round window membrane was manually opened through the transcanal access under careful irrigation and suction. A removable two-piece guide tube was placed in the tunnel to prevent contact of the electrode array with the drilled tunnel and to limit deviations or kinking during insertion (Figure 3c). The electrode array (Flex^{24}, MED-EL, Innsbruck, Austria) was inserted through the guide tube and into the cochlea under microscopic visualization. Full insertion of the electrode array was visually confirmed. The array lead was fixed at the round window niche, the excess lead was embedded within the mastoid cortex and wounds were closed.

2.5 Patient outcomes

Intraoperative implant telemetry demonstrated effective intra-cochlear placement of the electrode array: functional impedances were measured at all electrode contacts (average: 4.1kΩ, range: 2.6 to 6.6kΩ) and the electrically evoked compound action potentials recorded indicated effective auditory nerve stimulation. Postoperative CT imaging confirmed safe distances of the robotically drilled tunnel to the facial nerve and the chorda tympani to be approximately 1.0mm and 0.3mm, respectively. An angular insertion depth of 360 degrees of the electrode array was achieved (Figure 4b). CT evaluation indicated 11 of 12 intracochlear electrodes within the cochlea. Postoperative neuromonitoring showed unchanged facial nerve function, confirming that the integrity of the facial nerve was maintained during the robotic procedure. The patient was discharged from hospital one day postoperatively. Implant fitting of the patient is currently ongoing and audiological outcomes are reported for the 6 months post-activation session. As indicated by the postoperative CT, 11 electrodes were activated for stimulation. Evaluation of electrode impedance was within functional values and the aided sound field hearing threshold was 22 dB hearing level, averaged for the frequencies between 0.25 and 4 kHz. The patient had 50% word recognition in quiet tested at 65 dB sound pressure level with the Freiburg monosyllabic test.

3 Discussion

The past decade has resulted in an extensive body of research aiming to innovate cochlear implantation. Yet a true paradigm shift through comprehensive and consistent application of modern surgical technology that requires incorporation of robotics, image-guidance, and sensor technology has not occurred. In essence any technological innovation that seeks to supersede conventional Cochlear Implantation such as RCI must incorporate a set of fundamental elements that can deliver an improved CI procedure. These elements are 1) Computer-based patient-specific intervention planning, 2) Robotic middle ear access, 3) Robotic inner ear access and 4) Robotic electrode array insertion (Figure 1a). Some or all of the above elements have to be combined methodically to result in predictable and reproducible surgical and audiological outcomes of non-manual CI implantation technologies.

In this work, we have demonstrated a robotic implantation workflow model that combines parametric descriptions of all physical actions of and activities during a robotic treatment with patient data in order to specify elements that ensure a reproducible, consistent and safe procedure. This RCI workflow model may serve to facilitate successful development of radically new RCI iterations as well as confirm suitability of existing technological implementations.

We report our RCI procedure using a robotic, image-guided and sensor-controlled drill process. Our intent is to enable innovations to cochlear access and implantation methods that improve surgical outcomes, maintain safety, and widen treatment inclusion. This can be achieved through the use of process control and multi-layer safety management that can surpass the human limitations of sensing, dexterity, and execution capabilities of the manually operating surgeon. Robotic technology delivers a sub-millimetrically guided, heat

minimized drill process, complemented by bone-density to drill force mapping, intraoperative imaging and facial nerve monitoring.

The overall objective of this work is to demonstrate the viability of a model-based approach to RCI through the integration of the latest findings in image based planning, robotic image-guidance and auxiliary sensor technology to deliver a task-oriented surgical application that works beyond human proprioceptive skills. Our data confirm our hypothesis that a clinical application based on a systematic, comprehensive and universal robotic treatment model would be able to resolve challenges of precision, accuracy and safety. The resultant RCI platform solution, which is driven by a patient-specific planning and intervention algorithm, enabled the first procedure of RCI in a patient. We show here that a holistic RCI approach and predetermined universal workflow model provides for a personalized treatment outcome with a high degree of standardization and reproducibility while at the same time navigating patient-specific anatomy with robotic precision at the microsurgical scale.

A central safety aspect of our robotic cochlear implantation process is the dual approach to a position measurement system to ensure conformity with the image-based navigation model: first correlation of bone-density with drill forces to self-localize the robot created trajectory within the situs and second optical tracking, both implemented as mutually redundant features. In addition, automatic multipolar neuromonitoring tracks the structural integrity of the facial nerve during drilling independent of errors in the other safety mechanisms present. The clinical trial design underlying the procedure documented here also includes intraoperative cone-beam CT (CBCT) imaging to verify the correctness of the trajectory. Nonetheless, as clinical data are generated to support the resilience of the existing safety modalities, the robotic cochlear implantation procedure intended for clinical use will not require intraoperative imaging, avoiding the radiation burden and cost of this additional procedure.

In our hands, a stereotactically-guided robotic solution is potentially more resilient for Robotic Middle Ear Access (RMA) compared with template-guided and manually-drilled approaches (Labadie et al 2014) with respect to effective geometric accuracy (Schipper et al, 2004) active safety mechanisms (bone-density / drill force correlation, EMG). Such a tightly controlled drill process of our system delivers the drill and insertion vector path assigned by the personalized treatment plan.

This study did not include an assessment of Robotic Inner Ear Access (RIA), which has successfully been demonstrated in patients by Brett et al. The single function robotic technology described by Brett et al. is not extendable to perform Robotic Middle Ear Access (RMA), as RMA requires fundamentally different, image-guided control mechanisms. By contrast, in (Williamson et al 2014) we have demonstrated our system’s capability to carry out RIA following RMA using the integrated force-torque sensing technology (Williamson et al. 2014). Notwithstanding this and to comply with our approved trial protocol and experimental validation we have omitted this functionality in the ongoing clinical trial. Similarly, we have not investigated the third stage of RCI, namely Robotic Electrode Insertion (REI), because we consider this future work.

Atraumatic insertion of the electrode array into the cochlea is a critical part of the minimal invasive concept. We aim to reduce insertion-related trauma by (i) providing an optimized alignment of the insertion trajectory using the preoperative planning software, (ii) deploying the guide tube to constrict the array to the planned trajectory and to minimize kinking or lateral movement during insertion, (iii) speed and force controlled electrode array insertion through the guide tube into the cochlea using soft surgery haptics, and (iv) supervising the insertion through an auxiliary access. We are much encouraged by our findings from this study that an end-to-end, non-manual approach can be developed beyond cochlear access and are actively engaged in the investigation of a bias-minimized, non-manual insertion methodology. Atraumatic electrode insertion is an area of new research for us and a vital component of any robotic CI solution in the future, including our own.

Considering the effective drilling time of approx. <10 min, the brevity of which is offset by a number of longer, additional but compulsory steps such as: fiducial screw placement, computer-assisted planning and CBCT imaging prior to passing the facial nerve, the overall procedure time of RCI has to be addressed. In the same way we used a robotic treatment model to achieve safety, we will apply a model-based approach to progress our goal of an equal or shorter procedure time for RCI compared to conventional CI. For example, subject to final validation of the efficacy of all other safety mechanisms, we consider CBCT imaging and associated radiation exposure (0.3 mS) to be avoidable in the future. Because of the constrained size of the drill tunnel, the RCI approach is currently limited to lateral wall electrode arrays with diameters less than 1.5 mm. Clinical application of perimodiolar electrode arrays with the robotic approach would require array leads with smaller dimensions and insertion tools for stylet retraction mechanisms that can be deployed within the dimensions of the current RCI tunnel. We believe that the reporting of our RCI approach will encourage comprehensive implant technology R&D that will produce such CI feature evolution.

Future work will address robotic solutions for additional phases in procedural workflow. The control afforded by robotic drilling of the cochlear access, aims to minimize disturbances and trauma within the cochlea (Brett 2014). During robotic drilling the applicable force torque data is monitored for specific transients that correlate with a break through to the cochlear wall, which in turn forces the robot’s control system to stop the drill process much faster than a human could (Brett et al. 2014). Current work investigates the feasibility of our robot’s sensor systems to facilitate the integration of automatic cochlear wall drilling. Lastly, actuated and controlled insertion of the electrode array (Miroir et al 2012, Schurzig et al. 2012) is currently under investigation and may provide for consistent insertion speed and reduced insertion forces to reduce trauma to intracochlear structures.

The workflow of the RCI robotic cochlear procedure still requires extensive teamwork at all stages of the procedure: Pre-, intra, and post-operative stages are staffed in a multidisciplinary team structure: bioengineering, audiology, neuroradiology, surgery and allied health team members are present and active during the entire intervention, before and after. For clinical assessment and research purposes this is mandatory and appropriate. In routine clinical care this is prohibitive and makes any procedure unviable. The work required

to enable clinical adoption will have to address this and suitably iterate RCI-usability, which is a high priority objective for us.

Beyond the scope of cochlear implantation, we consider our technology also to be useful for local drug therapy in the inner ear, where the challenge of creating a reproducible, yet minimally invasive access to structures within the cochlea persists. In other applications, precision drilling in the lateral skull base could permit surgical approaches via several instruments and camera keyholes (Stenin et al. 2014), all joining near a specific target, effectively enabling minimally-invasive neurosurgical approaches in the skull-base.

4 Materials and methods

4.1 Robotic surgical system

We regard that the development of task specific surgical robotic manipulators optimized for a specific clinical use case has clear advantages over adapting ubiquitously available industrial robots (i.e. KUKA LWR etc.). These encompass task specificity by design, clinical integration functionality, early-stage safety considerations and flexibility to adapt the device and procedure to fit the specific requirements of clinical implementation. We aimed at developing a robotic solution that is safe for a human operator to carry (<10kg), directly attachable to an OR table and without the need for an additional cart. A five degree of freedom (DoF) serial manipulator and associated control hardware were specifically developed for application during minimally invasive microsurgical procedures on the lateral skull base. A serial kinematic design was chosen over a parallel (head-mounted) approach as it can be removed from and replaced in the surgical situs quickly at any time and without requiring re-registration or re-fixation. An overall manipulator arm length of 700 mm (base-to-tool-tip) was appointed, to provide optimal working volumes of approximately 100 × 100 × 100 mm^3 per configuration (left/right) and towards the side of the head being operated on at any given time.

Each of the manipulator joints consists of a motor/encoder/brake combination (axis 1-3: EC-max 30, axis 4 and 5: EC-max 22 Maxon Switzerland), and integrated gearboxes (HarmonicDrive, Japan; axis 1-3: CPL-17 and axis 4 and 5: CPL14) connected through a timing belt providing effective transmission ratios of 1:560 and 1:400 in axis 1-3 and axis 4-5 respectively. Inductive end switches are integrated in each joint to provide for a defined “zero-position” per axis. Digital motor control units (EPOS2 Module 36/2, Maxon, Switzerland) are directly integrated into the robot assembly (Robot base: Unit 1, link 3: Units 2 - 5). The setup provides for an effective Cartesian resolution of approximately 0.001 mm. A six-axis force-torque sensor (Mini-40, ATI, USA) and a semi-automatic tool quick release are fitted at the wrist. As well as an integrated voltage converter (24/5V) located in the base, the robot also houses a battery powered micro-controller (DSPIC33F, Microchip, USA) utilized to store all encoder values in non-volatile RAM during the systems intentional or emergency shut-down; these are then read back during repowering, eliminating the need for an initial calibration move at start-up in the absence of suitably sized absolute position encoders. Finally, several temperature sensors and accelerometers are placed in each of the links, monitoring temperature and motion status of the robot.

The manipulator structure itself was designed as a semi-monocoque structure [Airframe Handbook 1976] to effectively carry all tensile and compressive forces within its outer housing and without further internal frames that potentially contribute to additional weight. Subsequently, all links and joint components were computer-numerical-control milled from aluminum–copper alloy (Certal, EN AW-7022) and high-strength aluminum (EN AW-7075) providing a superior manipulator stiffness of 0.01 mmN^{-1} at a resulting minimum weight of 1.6 kg and 5.5kg for the monocoque structure and the complete robot system respectively.

Communication between the robot and the higher-level control system is enabled via two independent controller area network (CAN) buses. One bus links all digital motion controllers to the robots real-time control system. The second bus is used to query encoder values at startup as well as robot status and auxiliary sensor data. Electrical connection between the robot and navigation system is achieved via a combined power supply and bus cable (14 mm in diameter), effectively reducing clutter in the sterile area. Motor control is performed using a multi layered control system: low level current control is provided by the built-in motion controllers, with higher level position, velocity and interpolated-positioning control, as well as path planning, generated by proprietary, developed software in combination with the EPOS motion controllers. These higher-level control and path planning loops run and communicate with the motion controllers at 200 Hz, maximizing the available bandwidth of the utilized CAN bus. The developed higher level control software operates in a modified real time (RT-Preempt) Linux environment, on a 2.7GHz i7-based mini-ITX single board computer (MI980VF, iBase, USA). In addition to kinematic, control and path planning functions, the software interfaces with the higher-level navigation system, the integrated force-torque sensor and other auxiliary sensors, as well as the optical tracking system through a Transmission Control Protocol/Internet Protocol connection.

4.2 Auxiliary system components

A separate display and interface cart integrates computational hardware, power supply, signal conditioning/data acquisition hardware, medical grade safety relay and a touch screen user interface. Computational hardware consists of a Core i7 computer (quad-ore, 2.3 GHz, 8 GB, Windows 10) and a proprietary high-level control software, guiding the user through all relevant steps of the workflow.

An optical tracking system (Cambar B1, Axios3D, Germany) is attached at the robot base (Figure 5). The camera is capable of tracking custom LED-illuminated tracking references across its entire workspace with an accuracy of 0.05 ± 0.025 mm (Brun et al. 2013), at a tracking frequency of 60 Hz. Incoming tracking data (at 60Hz) is Kalman filtered to reduce latency and synchronized with the frequency of the robot's real-time control loop (100 Hz). Each of the tracking references contains 5 illuminated fiducials that are indirectly back-lit each by 4 IR LEDs (λ = 850 nm) to minimize orientation dependent variation of lighting intensity. Both trackers are synchronously strobed at the cameras exposure cycles with a duty cycle of 150 μs to avoid extensive heat built-up. The tracker fiducial geometry is optimized based on the available workspace and specific task, maximizing inter-fiducial distances while minimizing tracker obstructions. One tracker is attached to the patient's

skull via an adjustable bone anchor, the other rigidly mounted to the surgical drill hand piece.

Because to a lack of appropriate, commercially available solutions a proprietary drill system was designed and produced. Its stiffness ($0.01 mm N^{-1}$) and runout (0.018mm) values contribute significantly to meeting the accuracy requirements of the overall system. The brushless motor of the hand piece is also controlled via the robot control software through an EPOS motor control unit. The drill system is to be autoclaved for sterilization and is mechanically connected to the robot via the tool quick release. A custom drill bit with 1.8 mm (proximal, l=10mm) and 2.5 mm (distal, l=27mm) diameter sections was designed and produced in medical grade tungsten carbide for maximum tool stiffness. The overall geometric drilling accuracy and precision and excluding image-related errors has been verified to be 0.1±0.05 mm using a laser scanner based measurement stage while complete end-to-end system evaluation has revealed an accuracy of 0.15 ± 0.08 mm on n = 8 human cadaver specimens.

A clamp-like carbon-fiber headrest with three inflatable pressure pads was designed to reduce the relative motion between robot and patient during drilling (stiffness $<0.1 mm N^{-1}$) without the need for invasive percutaneous head fixation (i.e. Mayfield clamps). The head rest (Figure 3a) provides for non-invasive patient fixation while maintaining compatibility with intraoperative fluoroscopy based imaging systems. Together with the robot itself, the head-rest is mounted to the head side of the OR table via a rail mechanism.

4.3 Surgery planning

A software tool that assists in the identification and definition of the above-mentioned elements is derived from the preclinical image data and thereby produces a personalized patient specific treatment plan that includes the robotic drill plan and electrode insertion parameters (Gerber et al. 2014, Figure 6). Three-dimensional models of the relevant anatomy are created using semi-automated identification and annotation of the image data. Manual adjustments are performed by the user to ensure over-segmentation of structure boundaries, e.g. facial nerve. Software functionality is provided for the geometric definition of a drilling trajectory, as well as the definition of the various drilling phases. The trajectory is defined from the mastoid surface to the cochlea, bypassing all surrounding critical anatomical structures including the facial nerve, chorda tympani, ossicles and the posterior portion of the external auditory canal.

During manual optimization of the trajectory orientation, the software automatically calculates geometric distances from the trajectory to the surrounding modelled anatomy as well as angles between the trajectory and to the course of the cochlear basal turn to allow optimal implant electrode insertion. In a linkage step, the software detects fiducial screws that are placed in the patient's lateral skull base and are later used to intraoperatively register the plan to the patient. To accommodate accuracy requirements, detection of fiducial screws is automated and verified using fiducial volume accuracy and model-to-image matching variations (Gerber et al 2013). Comprehensive, general image quality tests are implemented to detect unacceptable image artifacts or insufficient image contrast levels. To conclude the

planning procedure, the most suitable implant electrode is selected based on the patient's cochlea parameters.

4.4 Instrument-flight like robot operation

The typical, human facial recess has a width of approximately 2.54 ± 0.5mm (Williamson et al 2017,), with the tunnel diameter required for the insertion of the current generation of electrodes being 1.8mm. Therefore, the accuracy required to consistently avoid the bounding nerves when drilling the minimally-invasive access tunnel is well beyond that achievable using existing navigation systems. Any clinically feasible, minimally invasive robotic access to the cochlea is dependent on an image guidance model that has a maximum geometric inaccuracy of less than 0.3 to 0.4 mm to warrant safe operation and sparing of the facial nerve. Here we set out the technical specifications that serve the purposes of geometric accuracy, redundant monitoring of the tool position independent of the image-guidance model and the electrophysiological stimulation and monitoring protocol. Patient-to-image registration involves physical digitization of topological coordinates of the patient's mastoid bone via bone-anchored fiducials, followed by algorithmic localization of the corresponding fiducial positions within the 3-D image data (i.e. in the image coordinate system). A least-squares-based algorithm (Veldpaus et al. 1988) is used to estimate a rigid transformation relating the physical and the image coordinate systems. Available geometric errors when measuring the fiducials' position, Fiducial Localization Error (FLE) are as low as 0.046 ± 0.029 mm and 0.153 ± 0.061 mm in physical and image space respectively (Gerber et al. 2013).

4.4.1 Precision image-guidance and visual servoing—During the drilling process a visual servoing scheme is used for command of the manipulator position (Agin 1979). The implemented vision-based controller employs multiple sources of sensor information to reduce latency and increase robustness. A Kalman filter fuses velocity information from the robots internal encoders (at 100Hz) with the camera position data (60Hz) (Williamson 2015). Active tracking is executed via optical references attached to the patient's head and the robot's end effector. This ensures critical compensation of minor patient movements (i.e. as a result of the finite stiffness of the head rest) and any remaining positional inaccuracies of the robot's internal differential position encoders (up to 0.3 mm in a 200^3 mm^3 cubic workspace).

In Bell et al. 2013 we have demonstrated a task specific end-to-end geometric accuracy of our drilling process to be 0.15 ± 0.08 mm in human cadaveric specimen. The accuracy was measured as the geometric displacement of a trajectory preoperatively defined in CT image data versus the drilled trajectory as identified in a postoperative CT scan. Rigorous minimization of all errors contributing to inaccuracy in the guidance model, such as optical tracking instrument calibration, fiducial localization in both the image and on the patient (Gerber et al. 2013) and were accomplished, together with a radical minimization of backlash and maximization of rigidity in all structural elements of the kinematic structure as well as the surgical drill system. Assuming a normal Gaussian distribution, the maximum geometric error of the robotic guidance system can be as low as 0.4 mm in 99.7% of all drilling attempts (3σ). This end-to-end geometric accuracy of an image guided robotic

system is the highest ever reported to our knowledge and is the base requirement to enable all other elements of the safety architecture.

Preliminary accuracy testing revealed deficiencies in standard surgical drilling hardware. Stainless steel drill bits deformed significantly under insignificant lateral loads with each traversal of an air cell in the mastoid bone. Factors such as tool deflection as result of diameter and backlash in the drilling unit itself further reduce the effective drilling accuracy. Thus, a backlash free drill spindle powered by a detachable surgical instrument drive (Osseopro, Bien Air, Switzerland) was developed and integrated in the robot's end-effector. Additionally, high rigidity tungsten carbide drill bits with 3 flutes were used to reduce tool bending (Louis Bélet, Switzerland).

4.4.2 Heat minimization during the drilling process—The second element of ensuring safety through system design is the implementation of a heat minimized drilling process. Drilling as close as 0.5 mm from the facial nerve likely creates exceptionally damaging amounts of heat energy. Labadie et al. 2014 have reported the incidence of a heat related facial palsy in a patient undergoing template based cochlear implantation. We have confirmed the possible danger of thermal damage to the facial nerve in an *in vivo* sheep study. It was found that drilling of the dense bone in the region of the facial nerve can lead to a harmful temperature rise (Feldmann et al. 2015). Therefore, we investigated the use of a novel drill bit specifically designed with an optimized geometry to minimize the amount of heat generated during the drilling process. Further iteration of the drill process included interval drilling at increments of 2 mm (in segments R1) and 0.5 mm (in segment R2) which was used to limit the accumulation of heat (Table 2). Additionally, at each increment the drill bit's flutes are flushed (1sec, 2ml) with saline solution. This prevents chip built-up, which potentially contributes to friction induced heat built-up. We therefore demonstrate in the current intervention, that the optimized drill bit and drilling process can maintain safe temperature levels while drilling at a 0.5 mm distance from the facial nerve (Feldmann et al. 2016). In addition, safe values for rotational and longitudinal drill speed have been established to be 1000 RPM and 0.5 mms^{-1} respectively to ensure the prerequisite temperature control. We assert that these features of the robotic device can maintain optimal compliance of the robotic CI procedure with the above parameters.

4.4.3 Bone density to drilling force correlation—In-situ confirmation of the robot's effective positional accuracy inside the human skull and after image co-registration has to date not been achieved in a clinical setting. Despite its superior general accuracy, image-guidance models are not fully reliable to be the exclusive informant for positional accuracy in a robotic surgical procedure. A secondary position measurement mechanism is essential to provide a physical crosscheck for the validity of the image-guidance model. We have developed a secondary localization method based on the correlation of drilling force and the variable bone density throughout the mastoid region. It allows the redundant prediction of the 6D pose of the drill trajectory independent of standard image guidance errors such as registration. It is assumed that any drill trajectory through the Mastoid results in a unique bone density profile along this trajectory. It is further assumed, that force/torque data

aqcuired during trajectory drilling optimally correlates with the executed trajectories' bone density profile.

Similiarity measures can be used to determine the best match from a given set of candidate trajectories that vary in position and orientation. These candidates are generated in an evenly spaced volume around the originally planned trajectory with variations in entry, target position and angles (to 2.5°) relative to the original trajectory. The similarity between the force and density profiles acts as a weighting factor, which is then used to calculate the weighted mean position of the tool (Figure 7). The initial implementation of this process demonstrated an accuracy of 0.29±0.21 mm when using force data only (Williamson et al. 2013). Subsequent improvements to the algorithm, including similarity metric, density extraction technique and workspace configuration, have led to increases in both accuracy and speed of the algorithm, with a current accuracy of 0.19±0.13 mm at a point 3 mm above the facial nerve observed. The specific layout of the alternative trajectories was initially defined based on the existing accuracy of the robotic system during the development of the algorithm. Subsequent evaluation has revealed that changes to the configuration of the alternative trajectories does not alter the accuracy of the algorithm, while allowing large errors (for example due to registration failures, as described in (Vernail et al. 2015) to be detected accurately.

4.4.4 Robot integrated neuromonitoring—The development of a suite of procedural safety components that would mitigate against the risk of structural damage to the facial nerve included a novel electromyography (EMG) facial nerve monitoring module. By measuring electromyogram signals in the facial muscles induced by electrical stimulation of the facial nerve through a dedicated stimulating probe, the distance of the trajectory to the facial nerve can be estimated to allow the drill-path to remain within safe limits. In the worst-case scenario, the procedure can be aborted based on the neuromonitoring data alone, before iatrogenic damage to the facial nerve would be sustained. Independent of all previously described safety mechanisms, this system is therefore to be considered the so-called "last line of defense" (Ansó et al. 2016). The system is based on a commercial electrical nerve stimulation and monitoring system (both ISIS, Inomed, Germany) and was fundamentally modified and customized with a multipolar stimulation probe/protocol (Figure 8) and proprietary software control system. This resulted in a dedicated RCI EMG system with the following task-specific functionalities:

- Sensitivity monitoring of the nerve (i.e. positive control, Holland 2002) established through a pair of surface stimulation electrodes located on the superficial branch of the facial nerve. The stimulus threshold values are expected to be in the range of 20 to 50 mA (monophasic pulses, duration = 250 μs) and are dependent on the electrode-electrolyte and skin contact impedance.
- Functional nerve status is continuously monitored via non-electrically triggered EMG (free-running EMG) responses to detect weak anesthesia conditions and potential nerve irritation due to, e.g. excessive mechanical pressure or temperature rise (Holland 2002).

Europe PMC Funders Author Manuscripts

- During drilling proximal to the facial nerve, the robot automatically evacuates from the drill tunnel, followed by manual insertion of the multi-electrode stimulation probe. Each of the four electrode configurations in the stimulation probe (B1, B2, B3 and monopolar) is then subject to an automatic stimulus threshold search. Stimulus threshold values above 1 mA likely indicate that the remaining bone thickness between the drill trajectory and the facial nerve is sufficiently protective, whereas values below 0.3 mA may indicate facial nerve dehiscence or absence of nerve bone covering. During electrical stimulation of the nerve, the amplitude of an electromyogram elicited signal is expected to be above 100 μV, and is composed of a complex polyphasic muscle action potential response. The stimulus threshold is the minimum intensity of the stimulating pulses that provided an EMG signal above 100 μV. Provided suitable electrode-tissue contact (impedance < 20 kΩ) are displayed, a reference scale is consulted (Table 3) to estimate the proximity to the facial nerve and give the system a go/no go command by the surgeon. Given a positive margin, the next drilling segment is executed by Go and the NM protocol is repeated with a final measurement as the facial nerve is cleared.
- Manual stimulation parameters for spot measurements permit verification of inconclusive data points generated during the stimulus threshold search automated EMG measurement protocol.

Data acquired in a sheep animal model (Ansó et al. 2016) have confirmed that this approach can reliably detect proximities of the drilled trajectory to the fallopian canal (i.e. the facial nerve) below 0.1 mm. We introduced the concept of *discretization* of the available drill-to-facial-nerve distance range into *safe* and *non-safe* zones where potentially hazardous collisions of the drill bit with the facial nerve can be identified with sufficient sensitivity and specificity (>95%). Histopathology of facial nerve sections from the in-vivo study suggested no relevant axonal injury of the facial nerve upon penetration and immediate (i.e. triggered by neuromonitoring) ceasing of robotic operation in the fallopian canal.

4.4.5 Intraoperative Cone-beam CT imaging—Although not part of the robotic system, intraoperative CBCT imaging aids in determining the drill trajectory pose in-situ and contributes to procedural safety. The clinical trial protocol for the procedure reported here mandates the use of intraoperative cone-beam CT imaging. We have established a protocol with a head scanner (xCAT, Xoran, USA) acquiring images of the patient's lateral skull base with a titanium rod inserted into the partially drilled access tunnel (action A1 of the robot plan). In the resulting scan, the automatically segmented titanium rod is extrapolated towards the target position (Figure 4a). In addition, the preoperative plan and images are co-registered (using a normalized mutual information metric) to allow geometric distance calculation from the segmented rod to the preoperatively modeled facial nerve. To allow intra-procedural decision-making in line with the clinical trial protocol, a neuroradiologist confirms a safe distance upon visual inspection of the intraoperative images. Our aim is to forgo intraoperative imaging in the RCI procedure eventually, to reduce patient irradiation, workflow complexity and cost.

Acknowledgments

Funding: This work was supported by the Swiss national science foundation (project NCCR Co-Me), Swiss Commission for technology and innovation (Project MIRACI 17618.1), the European Commission (project HEAR-EU, 304857), the Swiss Nano-Tera initiative (Project HearRestore), by MED-EL GmbH (Innsbruck, Austria) and CAScination AG (Bern, Switzerland)

References

[Agin 1979]. Agin, GJ. Real Time Control of a Robot with a Mobile CameraTechnical Note 179. SRI International; 1979 Feb.

[Airframes Handbook 1976]. Airframe and Powerplant Mechanics Airframe Handbook (Publication AC65-15A). Washington, DC: US Department of Transportation Federal Aviation Administration Standards Division; 1976. 4ISBN 0-16-036209-1

[Anso et al 2016]. Ansó J, Dür C, Gavaghan K, Rohrbach H, Gerber N, Williamson T, et al. A Neuromonitoring Approach to Facial Nerve Preservation During Image-guided Robotic Cochlear Implantation. Otol Neurotol. 2016; 37:89–98. [PubMed: 26649610]

[Bielamowicz et al 1988]. Bielamowicz S, Coker N, Jenkins H, Igarashi M. Surgical dimensions of the facial recess in adults and children. Arch Otolaryngol Head Neck Surg. 1988 May; 114(5):534–7. [PubMed: 3355691]

[Bell et al 2013]. Bell B, Williamson T, Gerber N, Gavaghan K, Wimmer W, Caversaccio M, Weber S. In Vitro Accuracy Evaluation of Image-Guided Robot System for Direct Cochlear Access. Otol Neurotol. 2013; 34:1284–90. [PubMed: 23921934]

[Brett et al 2014]. Brett PN, Du X, Zoka Assadi M, Coulson CJ, Reid AP, Proops DW. Feasibility study of a hand guided robotic drill for cochleostomy. BioMed Research International. 2014

[Brun et al 2013]. Brun, B; Williamson, T; Caversaccio, MD; Weber, S. Validation of custom active markers for use with a high accuracy tracking system. Conf Proc of 12. CURAC Annual congress 2013; 2013. 126–129.

[Clark et al 2014]. Clark JR, Leon L, Warren FM, Abbott JJ. Magnetic Guidance of Cochlear Implants: Proof-of-Concept and Initial Feasibility Study. ASME J Med Devices. 2012

[Close et al 2013]. Close A, Robertson C, Rushton S, et al. Comparative cost-effectiveness of robot-assisted and standard laparoscopic prostatectomy as alternatives to open radical prostatectomy for treatment of men with localised prostate cancer: a health technology assessment from the perspective of the UK National Health Service. Eur Urol. 2013; 64(3):361–369. [PubMed: 23498062]

[Conley et al 2011]. Conley DM, Singer SJ, Edmondson L, Berry WR, Gawande AA. Effective surgical safety checklist implementation. J Am Coll Surg. 2011 May.212(5):873. [PubMed: 21398154]

[Danilchenko et al 2011]. Danilchenko A, Balachandran R, Toennies JL, et al. Robotic mastoidectomy. Otol Neurotol. 2011 Jan.:11–16. [PubMed: 21042227]

[de Smet et al 2016]. de Smet MD, Meenink TC, Janssens T, Vanheukelom V, Naus GJ, Beelen MJ, Meers C, Jonckx B, Stassen JM. Robotic Assisted Cannulation of Occluded Retinal Veins. PLoS One. 2016 Sep 27.11(9)

[Dillon et al 2015]. Dillon NP, Balachandran R, Fitzpatrick JM, et al. A compact, bone - attached robot for mastoidectomy. J Med Devices. 2015:031003.

[Federspil et al 2003]. Federspil PA, Geisthoff UW, Henrich D, Plinkert PK. Development of the first force - controlled robot for otoneurosurgery. Laryngoscope. 2003 Mar.:465–471. [PubMed: 12616198]

[Feldmann et al 2015]. Feldmann A, Anso J, Bell B, Williamson T, Gavaghan K, Gerber N, et al. Temperature Prediction Model for Bone Drilling Based on Density Distribution and In Vivo Experiments for Minimally Invasive Robotic Cochlear Implantation. Ann Biomed Eng. 2015

[Feldmann et al 2016]. Feldmann A, et al. Reducing temperature elevation of robotic bone drilling. Medical Engineering and Physics. 2016; doi: 10.1016/j.medengphy.2016.10

[Gerber et al 2013]. Gerber N, Gavaghan Ka, Bell BJ, Williamson TM, Weisstanner C, Caversaccio M-D, et al. High-accuracy patient-to-image registration for the facilitation of image-guided robotic microsurgery on the head. IEEE Trans Biomed Eng. 2013; 60:960–8. [PubMed: 23340586]

[Gerber et al 2014]. Gerber N, Bell B, Gavaghan K, Weisstanner C, Caversaccio MD, Weber S. Surgical planning tool for robotically assisted hearing aid implantation. Int J Comput Assist Radiol Surg. 2014; 9:11–20. [PubMed: 23765213]

[Hori 2001]. Hori, K; Oyama, H; Ozaki, Y; Minato, K. Surgical cockpit system and effectiveness of its immersive environment. Proceedings of the 15th International Congress and Exhibition; Berlin, Germany. 2001 Jun 27-30.

[Huarte and Roland 2014]. Huarte R, Roland J. Toward hearing preservation in cochlear implant surgery. Curr Opin Otolaryngol Head Neck Surg. 2014; 22:349–352. [PubMed: 25101938]

[Holland 2002]. Holland NR. Intraoperative electromyography. J Clin Neurophysiol. 2002; 19(5):444–453. [PubMed: 12477989]

[Kobler et al 2015]. Kobler J-P, Nuelle K, Lexow GJ, et al. Configuration optimization and experimental accuracy evaluation of a bone - attached, parallel robot for skull surgery. Int J Comput Assist Radiol Surg. 2015:421–436. [PubMed: 26410844]

[Koethe et al 2014]. Koethe Y, Xu S, Velusamy G, Wood BJ, Venkatesan AM. Accuracy and efficacy of percutaneous biopsy and ablation using robotic assistance under computed tomography guidance: a phantom study. Eur Radiol. 2014 Mar; 24(3):723–30. [PubMed: 24220755]

[Kratchman et al 2011]. Kratchman LB, Blachon GS, Withrow TJ, et al. Design of a bone - attached parallel robot for percutaneous cochlear implantation. IEEETrans Biomed Eng. 2011 Oct.:2904–2910.

[Labadie et al 2005]. Labadie RF, Chodhury P, Cetinkaya E, Balachandran R, Haynes DS, Fenlon MR, Jusczyzck AS, Fitzpatrick JM. Minimally invasive, image-guided, facial-recess approach to the middle ear: demonstration of the concept of percutaneous cochlear access in vitro. Otol Neurotol. 2005 Jul; 26(4):557–62. [PubMed: 16015146]

[Labadie et al 2014]. Labadie RF, Balachandran R, Noble JH, Blachon GS, Mitchell JE, Reda FA, Dawant BM, Fitzpatrick JM. Minimally invasive image-guided cochlear implantation surgery: first report of clinical implementation. Laryngoscope. 2014 Aug; 124(8):1915–22. [PubMed: 24272427]

[Lunsford et al 1989]. Lunsford LD, Flickinger J, Lindner G, Maitz A. Stereotactic radiosurgery of the brain using the first United States 201 cobalt-60 source gamma knife. Neurosurgery. 1989; 24:151–159. [PubMed: 2645538]

[Marcus et al 2013]. Marcus H, Nandi D, Darzi A, Yang GZ. Surgical robotics through a keyhole: from today's translational barriers to tomorrow's “disappearing” robots. IEEE Trans Biomed Eng. 2013 Mar; 60(3):674–81. [PubMed: 23372075]

[Miroir et al 2012]. Miroir M, Nguyen Y, Kazmitcheff G, Ferrary E, Sterkers O, Grayeli AB. Friction force measurement during cochlear implant insertion: application to a force-controlled insertion tool design. Otol Neurotol. 2012; 33:1092–100. [PubMed: 22772019]

[Noble et al 2012]. Noble JH, Gifford RH, Labadie RF, Dawant BM. Statistical shape model segmentation and frequency mapping of cochlear implant stimulation targets in CT. Med Image Comput Comput Assist Interv. 2012; 15(Pt 2):421–8. [PubMed: 23286076]

[Pearle et al 2009]. Pearle AD, Kendoff D, Stueber V, Musahl V, Repicci JA. Perioperative management of unicompartmental knee arthroplasty using the MAKO robotic arm system (MAKOplasty). Am J Orthop. 2009; 38(Suppl. 2):16–19. [PubMed: 19340378]

[Pile et al 2014]. PileWanna, GB; Simaan, N. Force-based flexible path plans for robotic electrode insertion. 2014 IEEE International Conference on Robotics and Automation (ICRA); Hong Kong. 2014. 297–303.

[Pile et al 2016]. Pile J, Wanna GB, Simaan N. Robot-assisted perception augmentation for online detection of insertion failure during cochlear implant surgery. Robotica. 2016:1–18.

[Rajan et al 2013]. Rajan G, Kontorinis G, Kuthubutheen J. The effects of insertion speed on inner ear function during cochlear implantation: a comparison study. Audiol Neurootol. 2013; 18:17–22. [PubMed: 23006502]

[Reza et al 2010]. Reza M, Maeso S, Blasco JA, Andradas E. Meta-analysis of observational studies on the safety and effectiveness of robotic gynaecological surgery. Br J Surg. 2010 Dec; 97(12): 1772–83. [PubMed: 20949554]

[Schipper et al 2004]. Schipper J, Klenzner T, Aschendorff A, Arapakis I, Ridder GJ, Laszig R. Navigation-controlled cochleostomy. Is an improvement in the quality of results for cochlear implant surgery possible? HNO. 2004 Apr; 52(4):329–35. [PubMed: 15014891]

[Schurzig et al 2012]. Schurzig D, Labadie RF, Hussong A, Rau TS, Webster RJ. Design of a tool integrating force sensing with automated insertion in cochlear implantation. IEEE/ASME Trans Mechatronics. 2012; 17:381–9. [PubMed: 23482414]

[Shademan et al 2016]. Shademan A, Decker RS, Opfermann JD, Leonard S, Krieger A, Kim PCW. Supervised autonomous robotic soft tissue surgery. Sci Transl Med. 2016; 8:337ra64.

[Smith et al 2016]. Smith JA, Jivraj J, Wong R, Yang V. 30 Years of Neurosurgical Robots: Review and Trends for Manipulators and Associated Navigational Systems. Ann Biomed Eng. 2016 Apr; 44(4):836–46. [PubMed: 26467553]

[Sommer 2014]. Sommer KJ. Pilot training: What can surgeons learn from it? Arab J Urol. 2014 Mar; 12(1):32–5. [PubMed: 26019919]

[Staecker et al 2001]. Staecker H, O'malley BW, Eisenberg H, Yoder BE. Use of the Landmarxtrade mark Surgical Navigation System in Lateral Skull Base and Temporal Bone Surgery. Skull Base. 2001 Nov; 11(4):245–55. [PubMed: 17167627]

[Stenin et al 2014]. Stenin I, Hansen S, Becker M, Sakas G, Fellner D, Klenzner T, Schipper J. Minimally invasive multiport surgery of the lateral skull base. Biomed Res Int. 2014:7.

[Veldpaus et al 1988]. Veldpaus FE, Woltring HJ, Dortmans LJ. A least-squares algorithm for the equiform transformation from spatial marker co-ordinates. J Biomech. 1988 Jan; 21(1):45–54. [PubMed: 3339026]

[Venail et al 2015]. Venail F, Bell B, Akkari M, Wimmer W, Williamson T, Gerber N, et al. Manual Electrode Array Insertion Through a Robot-Assisted Minimal Invasive Cochleostomy: Feasibility and Comparison of Two Different Electrode Array Subtypes. Otol Neurotol. 2015; 36:1015–22. [PubMed: 25853609]

[Wimmer et al 2014a]. Wimmer W, Venail F, Williamson T, Akkari M, Gerber N, Weber S, et al. Semiautomatic cochleostomy target and insertion trajectory planning for minimally invasive cochlear implantation. Biomed Res Int. 2014; 2014doi: 10.1155/2014/596498

[Wimmer et al 2014b]. Wimmer W, Bell B, Huth ME, Weisstanner C, Gerber N, Kompis M, et al. Cone beam and micro-computed tomography validation of manual array insertion for minimally invasive cochlear implantation. Audiol Neurootol. 2014; 19:22–30. [PubMed: 24280962]

[Williamson 2013]. Williamson TM, Bell BJ, Gerber N, Salas L, Zysset P, Caversaccio MD, et al. Estimation of tool pose based on force-density correlation during robotic drilling. IEEE Trans Biomed Eng. 2013; 60:969–76. [PubMed: 23269744]

[Williamson et al 2014]. Williamson T, Du X, Bell B, Coulson C, Caversaccio M, Proops D, Brett P, Weber S. Mechatronic feasibility of minimally invasive, atraumatic cochleostomy. Biomed Res Int. 2014; 2014

[Williamson 2015]. Integrated sensing and control for robotic microsurgery on the lateral skull base. Phd Thesis, University of Bern; Switzerland: 2015.

[Williamson 2017]. Williamson T, Gavaghan K, Gerber N, Weder S, Anschuetz L, Wagner F, Weisstanner C, Mantokoudis G, Caversaccio M, Weber S. A population statistics approach for safety assessment in robotic cochlear implantation. Otol Neurotol. 2017; 38(5):759–764. [PubMed: 28196000]

[Xia et al 2008]. Xia T, Baird C, Jallo G, et al. An integrated system for planning navigation and robotic assistance for skull base surgery. Int J Med Robot Comput Assist Surg. 2008 Dec.:321–330.

[Xiong et al 2012]. Xiong B, Ma L, Zhang C. Robotic versus laparoscopic gastrectomy for gastric cancer: a meta-analysis of short outcomes. Surg Oncol. 2012; 21(4):274–280. [PubMed: 22789391]

[Zhang et al 2010]. Zhang, Jian. Inroads toward robot-assisted cochlear implant surgery using steerable electrode arrays. Otology & Neurotology. 2010; 31(8):1199–1206. [PubMed: 20864880]

Summary

Image-guided robotic surgery, designed for operating on small structures, is demonstrated for cochlear implantation

Europe PMC Funders Author Manuscripts

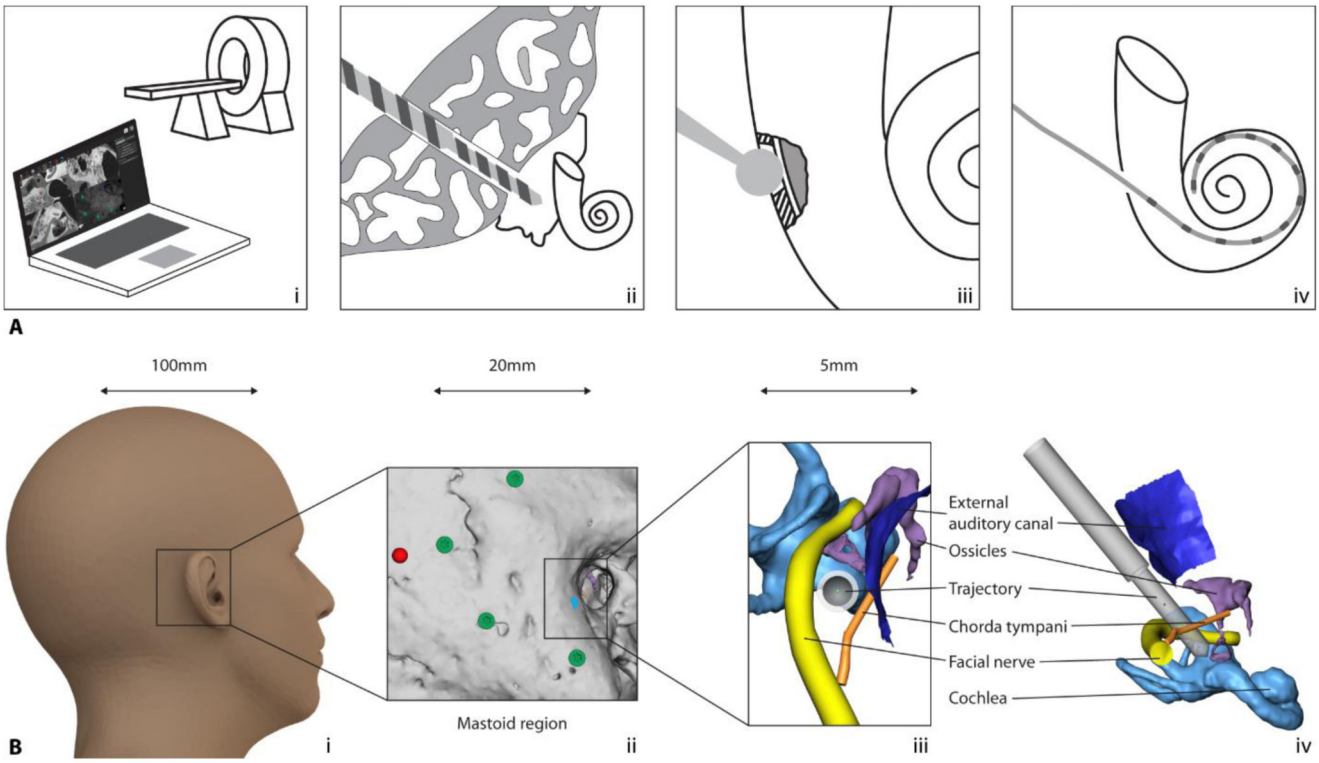

Figure 1. Robotic cochlea implantation RCI.

(**A**) Elements of RCI: (i) computer-based patient-specific intervention planning, (ii) RMA, (iii) RIA, and (iv) robotic electrode array insertion. (B) Scale of RCI: A 1.8-mm trajectory to be planned and drilled starting from behind the ear (i), through the mastoid bone (ii) bypassing critical structures at <1-mm proximity and toward the inner ear. Trajectory viewed along its axis (iii) and from the side (iv).

Europe PMC Funders Author Manuscripts

Europe PMC Funders Author Manuscripts

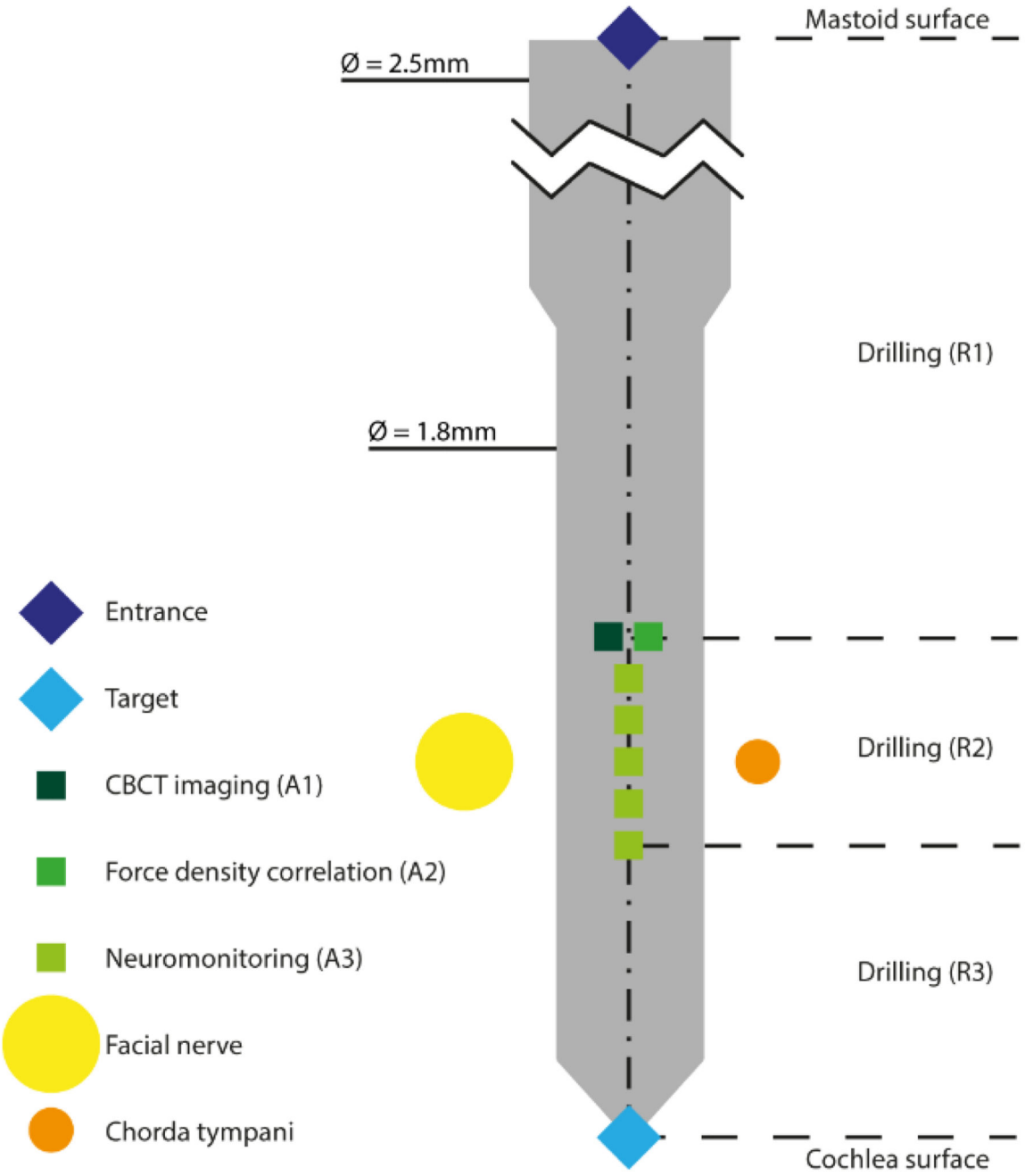

Figure 2. Visual representation of the treatment model for RMA.
Procedural elements and risk mitigation activities of an RCI plan.

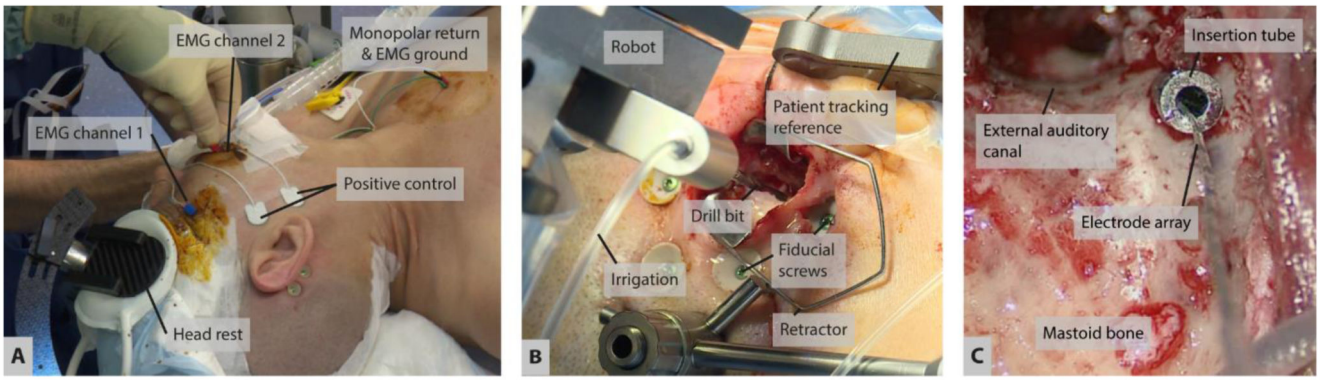

Figure 3. Surgical preparation, robotic drilling, and implant insertion.

(**A**) Noninvasive, steady placement of the patient's head on pressure pads attached to a carbon fiber support structure. Electrodes for neuromonitoring of the facial nerve are attached to facial muscles. (**B**) The robotic drill accesses the situs through a 20-mm incision. (**C**) Using an insertion tube, the CI electrode is inserted through the 1.8-mm keyhole into the cochlea.

Europe PMC Funders Author Manuscripts

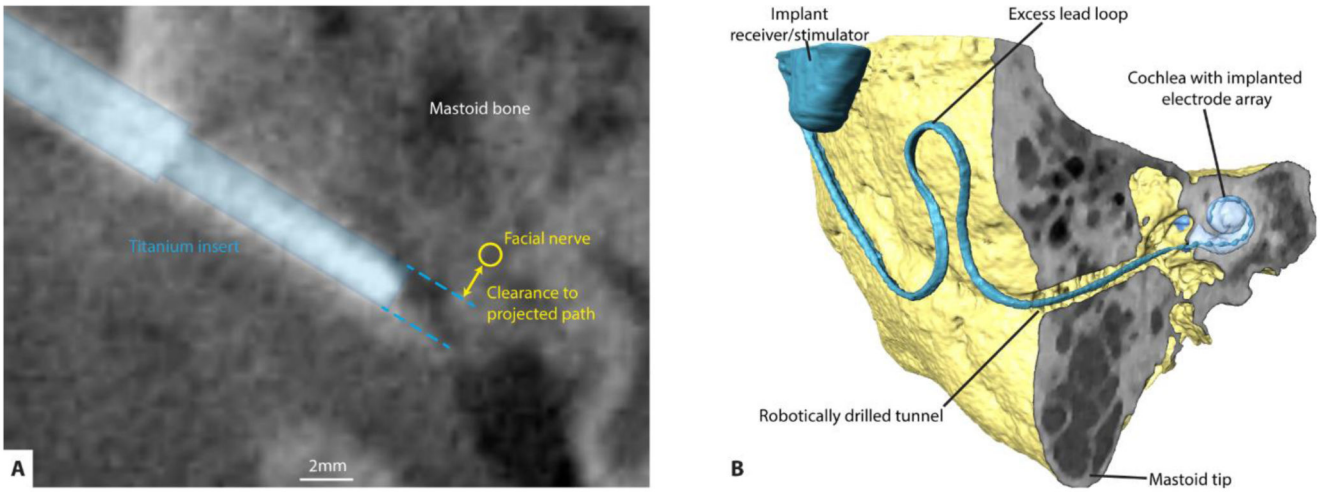

Figure 4. Confirmation of safe passage and postoperative situation.

(**A**) Intraoperative CBCT imaging allows delineation of the trajectory and the facial nerve. A neuroradiologist manually confirms sufficient distance between the trajectory and the facial nerve. (**B**) Inserted electrode array, excess lead placement, and final implant position as measured in postoperative CT imaging.

Europe PMC Funders Author Manuscripts

Europe PMC Funders Author Manuscripts

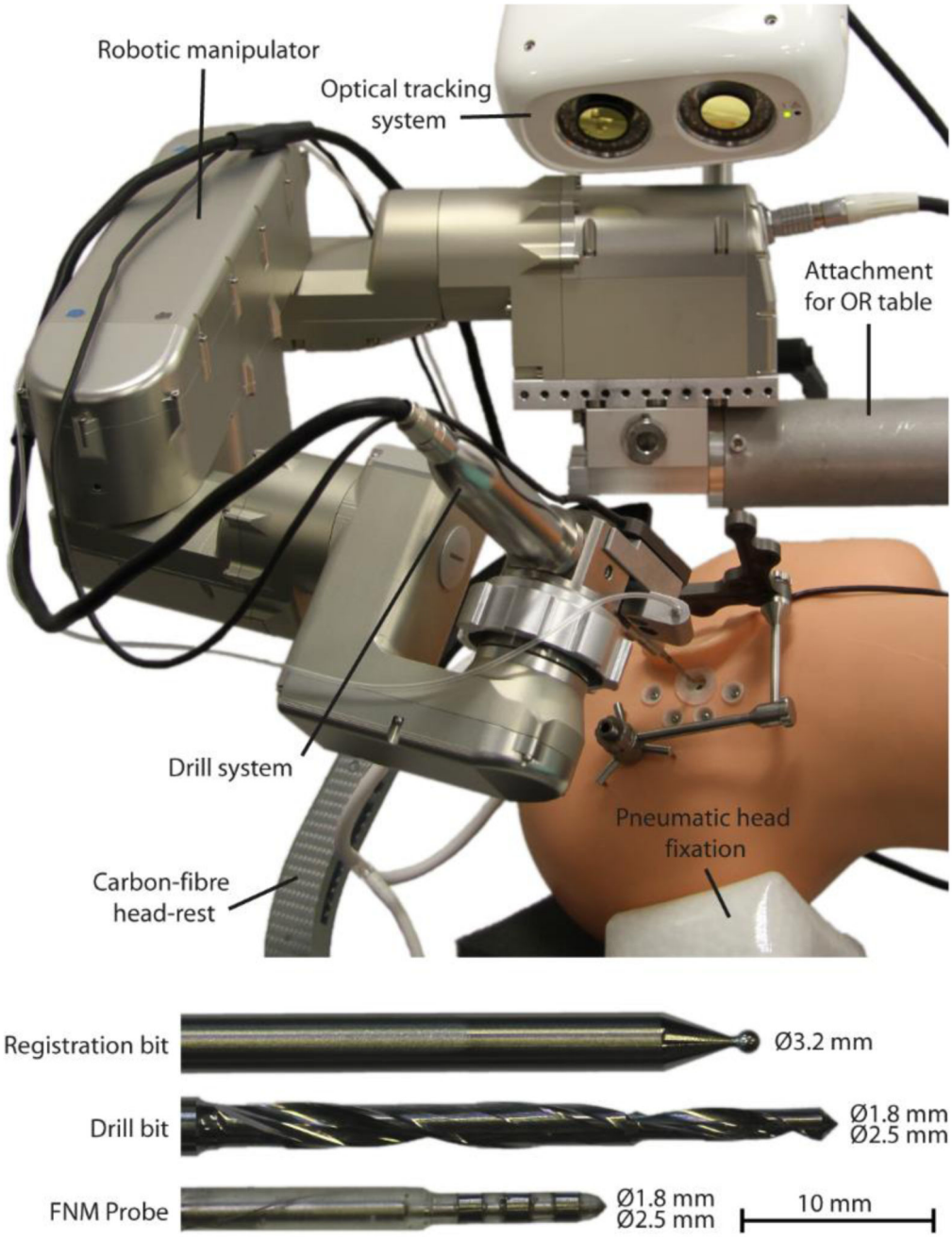

Figure 5. System overview.
Highlighting all relevant robotic, stereotactic, and surgical instrument components.

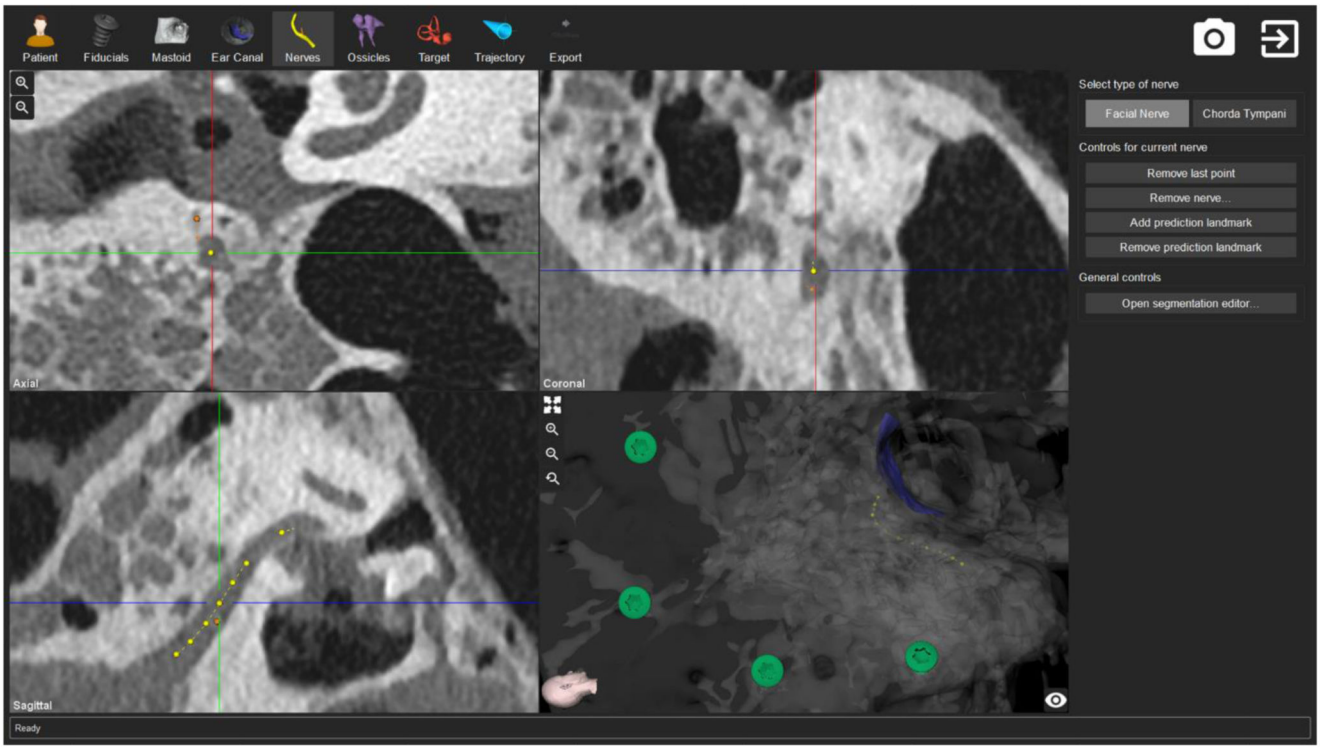

Figure 6. Planning the intervention.

The planning software tool allows for general image segmentation (i.e., identification of the fiducial screws, in green), segmentation of anatomy (i.e., facial nerve, in yellow), and parametrization of the general treatment plan.

Europe PMC Funders Author Manuscripts

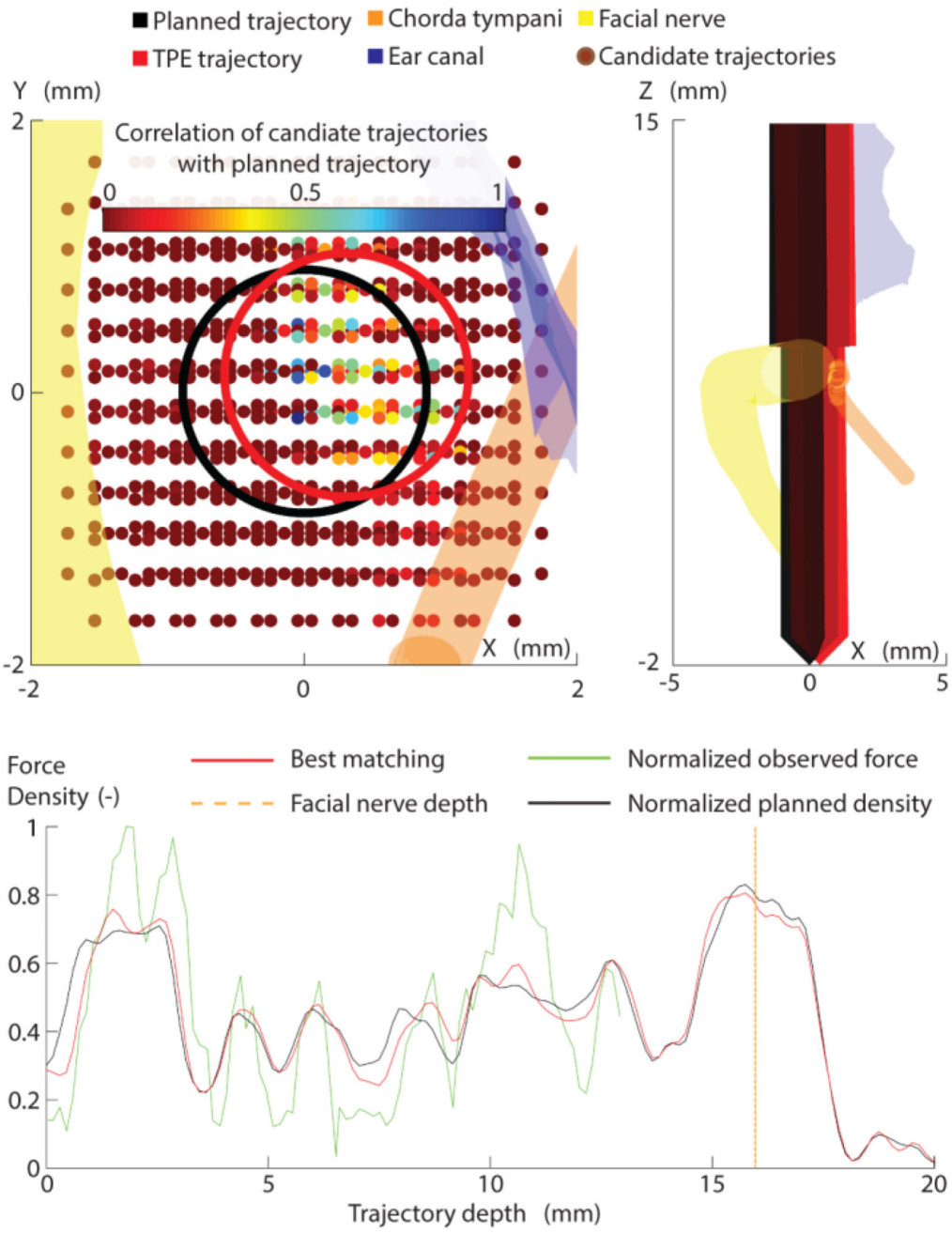

Figure 7. Pose estimation using drill force and bone density.

Computation of the trajectory pose using a correlation of bone density (from CT) and drill force (recorded during drilling process).

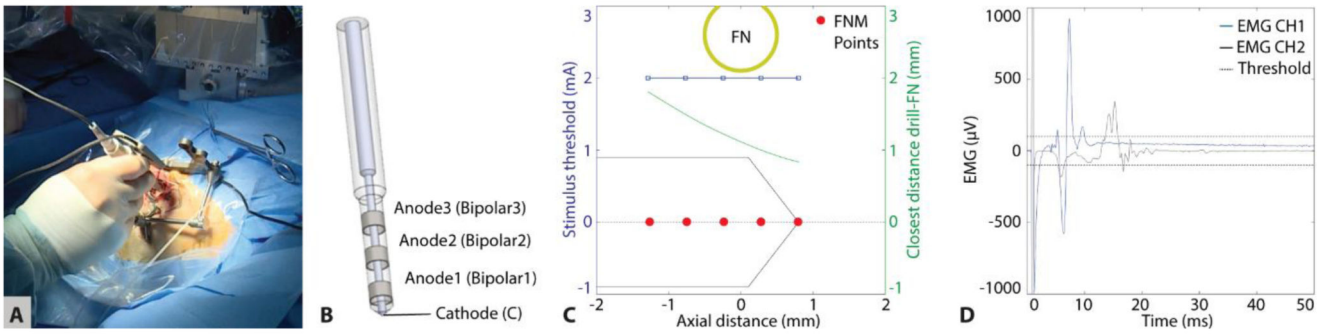

Figure 8. Neuromonitoring of the facial nerve during robotic drilling.

(**A**) Optically tracked stimulation probe inserted in the drilled tunnel near the facial nerve before application of an automatic protocol through four channels of the probe. (**B**) Probe with cathode to anode distances to be di = 2, 4, 7 mm ($Anode_i$), and monopolar stimulation enabled by a far-field needle electrode (superficial to the sternum). (**C**) After automatic stimulation between 0.2 and 2 mA, EMG responses only appeared at 2 mA and the monopolar configuration, suggesting a safe drilling passage at facial nerve distances above 0.7 mm. (**D**) Example of electrically elicited EMG signals during drilling, showing amplitude range and polyphasic nature of responses.

Europe PMC Funders Author Manuscripts

Europe PMC Funders Author Manuscripts

Table 1

RMA model.

The model's elements consist of robotic activities (R), risk mitigation actions (A), and manual activities (M).

Element	Description	Parameters
R1	Robotic drilling from Mastoid surface to 3mm before the level of the facial nerve	X_{Start}, X_{End} Drilling interval = 2 mm rpm: 1000 Irrigation: 15 ml/minute Guiding: Optical tracking Velocity = 0.5 mm/s Drill Ø: 2.5 mm
A1	Intraoperative CBCT imaging	Field of view: 80 × 80 × 80 mm^3 Resolution: 0.156 × 0.156 mm^2, slice thickness 0.2 mm
A2	Bone-density analysis	Candidate trajectories: n = 2000 Volume of interest: 3 × 3 × 30 mm around planned trajectory
R2	Robotic drilling lateral to the facial nerve	X_{Start}, X_{End} Drilling interval = 0.5mm rpm: 1000 Irrigation: 15 ml/minute Guiding: Optical tracking Velocity = 0.5 mm/s Drill Ø: 1.8 mm
A3	Electromyography facial nerve monitoring	Measurement points: 5 Distance between points: 0.5 mm Monopolar channels: 1 Bipolar channels: 3 Pulse duration = 250 μs Intensities per channel = 0.2 … 2 mA (ΔI = logarithmic)
R3	Facial nerve to 2 mm before the round window	X_{Start}, X_{End} Drilling interval = 2mm rpm: 1000 Irrigation: 15 ml/minute Guiding: Optical tracking Velocity = 0.5 mm/s Drill Ø: 1.8 mm
R4	Cochlea opening (manual)	Guiding: Force feedback Bur Ø 1.0 mm
M5	Electrode insertion (manual)	Choice of implant: $Flex^{24}$ (MED-El) Length of insertion: 360°

Europe PMC Funders Author Manuscripts

Table 2

Robotic access plan.

R, robotic actions; A, risk mitigation actions.

Element	Description	Duration
R1	Drilling commenced from the lateral skull surface to 3 mm before the facial nerve	4 min
A1	Effective trajectory pose measurement using drill force-to-bone density correlation. Sufficient lateral space of the trajectory from the facial nerve and the chorda tympani was confirmed to be 1.0 and 0.3mm, respectively	1 min
A2	Acquisition of intraoperative CT yielded sufficient lateral space of the trajectory from the facial nerve and the chorda tympani to be 1.0 and 0.2mm respectively	55 min
R2	Passing at the critical safe distance to both the facial nerve (<1.0mm) and the chorda tympani (0.3mm). Intervals of the robotic drilling were shortened (0.5 versus 1mm) to mitigate for heat buildup	3 min
A3	EMG facial nerve monitoring was performed at six positions and every 0.5mm increment in depth. At all positions, neuromonitoring yielded a distance of the trajectory safe for the facial nerve	5 × 2 min
R3	Drilling phase R3 commenced 3 mm past the level of the facial nerve and concluded 2 mm before the planned target location on the cochlea within the middle ear cavity	3 min

Europe PMC Funders Author Manuscripts

Table 3

EMG decision table based on stimulus threshold values above (0) or below (1) 0.35 mA.

Electrode configuration				Estimated distance ranges drill to facial nerve (mm)		Decision	Confidence
Bipolar			Monopolar	Min	Max		
d = 2 mm	d = 4 mm	d = 7 mm					
0	0	0	0	0.7		Continue to drill	> 95 %
0	0	0	1	0.6	0.7	Continue to drill	> 95 %
0	0	1	0	0.4	0.6	Continue to drill	< 95 %
0	0	1	1	0.4	0.7	Continue to drill	> 95 %
0	1	0	0	0.1	0.4	Further assessment required	< 95 %
0	1	0	1	0.1	0.4		< 95 %
0	1	1	0	0.1	0.4		< 95 %
0	1	1	1	0.1	0.4	Critical to abort	> 95 %
1	0	0 or 1	0 or 1	0	0.1	Abort RCI	< 95 %
1	1	0 or 1	0 or 1	0	0.1	Abort RCI	> 95 %